Journal of Science: Advanced Materials and Devices 10 (2025) 100971

Contents lists available at ScienceDirect

Journal of Science: Advanced Materials and Devices

journal homepage: www.elsevier.com/locate/jsamd

Research Article

Synergistic A-site co-doping of $(Na_{1/2}Bi_{1/2})_xBa_{1-x}Zn_{1/3}Nb_{2/3}O_3$ perovskites: doping mechanisms, microstructure and impedance studies

Y. Feng [a], A.T.Z. Lim [b], M. Lu [c], J. Sun [d], K.Y. Chan [e], S. Ghotekar [f], D. Zhou [g,*], D.C. Sinclair [h,**], K.B. Tan [a,***]

[a] Department of Chemistry, Faculty of Science, Universiti Putra Malaysia, Serdang, 43400, Selangor, Malaysia
[b] Department of Science and Technology, Faculty of Humanities, Management and Science, Universiti Putra Malaysia Sarawak, Bintulu, 97008, Sarawak, Malaysia
[c] The Joint Laboratory of MXene Materials, Key Laboratory of Functional Materials Physics and Chemistry of the Ministry of Education, Jilin Normal University, Changchun, Jilin, 130103, China
[d] School of Materials Science and Engineering, Nankai University, Tianjin, 300350, China
[e] Faculty of Artificial Intelligence and Engineering, Multimedia University, Persiaran Multimedia, 63100, Cyberjaya, Selangor, Malaysia
[f] Centre for Herbal Pharmacology and Environmental Sustainability, Chettinad Hospital and Research Institute, Chettinad Academy of Research and Education, Kelambakkam, 603103, Tamil Nadu, India
[g] Electronic Materials Research Laboratory, Key Laboratory of the Ministry of Education and International Center for Dielectric Research, School of Electronic Science and Engineering, Xi'an Jiaotong University, Xi'an, 710049, Shaanxi, China
[h] School of Chemical, Materials and Biological Engineering, University of Sheffield, Sir Robert Hadfield Building, Mappin Street, Sheffield, S1 3JD, UK

ARTICLE INFO

Keywords:
Perovskites
Phase evolution
Densification and dielectric properties

ABSTRACT

This study explores the novel synergistic co-doping of $(Na_{1/2}Bi_{1/2})^{2+}$ ions into the A-sites of $Ba(Zn_{1/3}Nb_{2/3})O_3$ (BZN) perovskites to optimise dielectric properties and reduce sintering temperatures. Polycrystalline $(Na_{1/2}Bi_{1/2})_xBa_{1-x}Zn_{1/3}Nb_{2/3}O_3$ ceramics (x = 0.1–0.4) were synthesised via solid-state reaction, achieving dense microstructures with relative densities exceeding 92 %. The presence of $Na_{0.13}Bi_{1.87}O_{2.87}$ and $ZnNb_2O_6$ transient phases facilitated a significant reduction in sintering temperature from 1200 °C (x = 0.1) to as low as 950 °C (x = 0.4). XRD, Rietveld refinement and TEM confirmed the formation of phase-pure cubic perovskites with $Pm\bar{3}m$ symmetry. Dielectric studies revealed enhanced room-temperature relative permittivity (ε′) and optimised dielectric loss (tan δ), attributed to dipole polarisation induced by $6s^2$ lone-pair electrons of Bi^{3+} and improved grain size. Notably, the composition, x = 0.2 exhibited the lowest tan δ (~0.0096 at 1 MHz) and highest electrical resistance, representing the optimal balance of dielectric performance. Impedance spectroscopy analysis revealed grain-dominated electrical processes and reduced oxygen vacancies, thereby corroborating the correlation between composition, microstructure and electrical properties. This work highlights the functionality of $(Na_{1/2}Bi_{1/2})^{2+}$ co-doping to enhance the dielectric performance of BZN perovskites while achieving optimal density at reduced sintering temperatures, thus rendering them suitable for applications in Low-Temperature Co-Fired ceramic (LTCC) for advanced electronic devices.

1. Introduction

With the rapid progress and development of 5G networks, electric vehicles and portable devices, there has been a significant surge in the demand for cutting-edge electronic components characterised by low dissipation, high capacity, miniaturisation and seamless integration [1]. Complex perovskites containing Ba, distinguished by their excellent dielectric properties and exceptional frequency and temperature stability, hold substantial promise for microelectronics [2,3]. Among these, the solid solutions of $Ba^{2+}(B^{2}_{1/3}{}^{+}B^{5}_{2/3}{}^{+})O_3$ (B^{2+} = Mg, Ni, Co and Zn; B^{5+} = Ta and Nb) have garnered considerable attention due to their extremely low tan δ, e.g., the perovskites in the $Ba(Zn_{1/3}Ta_{2/3})O_3$ (BZT) and $Ba(Mg_{1/3}Ta_{2/3})O_3$ (BMT) systems [4,5]. Considering higher cost and poor sinterability of Ta_2O_5, the niobium analogue, $Ba(Zn_{1/3}Nb_{2/3})O_3$

* Corresponding author.
** Corresponding author.
*** Corresponding author.
E-mail addresses: zhoudi1220@xjtu.edu.cn (D. Zhou), d.c.sinclair@sheffield.ac.uk (D.C. Sinclair), tankarban@upm.edu.my (K.B. Tan).

https://doi.org/10.1016/j.jsamd.2025.100971
Received 19 May 2025; Received in revised form 5 August 2025; Accepted 7 August 2025
Available online 9 August 2025

(BZN) is preferable, particularly due to its modest ε' of 41, low tan δ in the order of 10^{-4}-10^{-3} and adjustable temperature coefficient of capacitance (τ_{cc}) of −68.8 ppm/°C, thus making it a promising candidate for microwave components and capacitors [6,7].

In the recent past, BZN perovskites have been the subject of extensive research, encompassing the utilisation of various synthesis methods, chemical doping approaches and ordered domain engineering. Notably, the stoichiometric deviation in BZN perovskites has demonstrated a significant impact on B-site cation ordering, sintering behaviour and dielectric properties. Even a minimal concentration of Ba deficiency can lead to enhanced sinterability and an increased degree of ordering for B-site cations in $Ba_{0.99}(Zn_{1/3}Nb_{2/3})O_3$ [8]. Furthermore, Zn-rich non-stoichiometric $Ba(Zn_{1/3}Nb_{2/3})_{1-x}Zn_xO_3$ ($0.01 < x < 0.04$) perovskites, synthesised at 1500 °C via solid-state reaction, have exhibited a remarkably low tan δ of 5.5×10^{-4} at $x = 0.02$, attributable to the enhanced intrinsic packing fraction [9]. In other related studies, the incorporation of B_2O_3 and CuO has facilitated a substantial reduction in the sintering temperature of BZN perovskites, reaching 900 °C and 875 °C, respectively. These alterations are attributed to liquid-phase assisted sintering as a result of the melting process of secondary phases, e.g., BaB_4O_7, BaB_2O_4 and $BaCu(B_2O_5)$ [10]. It is noteworthy that the BZN perovskite, with addition of CuO, exhibited an ε' of 36 and a near-zero temperature coefficient of resonant frequency (τ_f) of 21 ppm/°C.

On the other hand, the enhanced B-site cation ordering in BZN perovskites was discovered to be a critical factor in minimising tan δ [11]. Typically, annealing below the ordering-disordering phase transition temperature effectively promotes 1:2 ordering. Recently, BZN perovskites with excellent dielectric properties ($Q \times f = 89{,}600$ GHz and $\tau_f = 22$ ppm/°C) have been successfully synthesised using the novel digital light processing (DLP) technique followed by annealing at 1300 °C for 24 h, attributed to the enhanced B-site 1:2 ordering degree [12]. However, the potential Zn volatilisation and oxygen depletion during annealing could adversely impact dielectric properties, necessitating alternative low-temperature synthesis methods. Recently, a significant increase in $Q \times f$ values from 21,200 to 69,300 GHz was observed in Ba$(Co_{0.7}Zn_{0.3})_{1/3}Nb_{2/3}O_3$ (BCZN) with 0.2 wt% CuO [13]. This composition also demonstrated an improved 1:2 ordering due to the formation of quasi-liquid CuO-xCu_2O layers after firing at 1300 °C for 10 h. Despite these advancements, excessively high sintering temperatures above 1300 °C should be avoided, as Zn or Ba evaporation may result in lattice defects; while, the lowered firing temperature enhances compatibility with Ag electrodes for Low-Temperature Co-Fired Ceramics (LTCC) applications. This also highlighted an urgent need to address this firing issue, particularly since most studies were still primarily focused on the B-site substitution instead of A-site modification.

Substitution on the larger A-site cations in perovskites is also important as this significantly impacts their crystallo-chemical structure and dielectric properties [14,15]. In this regard, Ca-doped $Ba_{1-x}Ca_x(Zn_{1/3}Nb_{2/3})O_3$ ($0 \le x \le 0.2$) perovskites exhibited a phase transition from a cubic to an orthorhombic structure at $x \ge 0.05$, exhibiting a high $Q \times f$ value of 37.1×10^3 MHz for $x = 0.15$ [16]. The reactive and volatile Bi_2O_3, with a low volatilisation temperature of ~825 °C, has been extensively applied as a sintering aid in LTCC, including the systems $Sr_{1-x}(Na_{1/2}Bi_{1/2})_xBi_2Nb_2O_9$ [17] and $Sr_{1-x}(Na_{1/2}Bi_{1/2})_xTi_{0.99}Mn_{0.01}O_3$ [18]. Additionally, a higher ε' was achievable due to the local structural distortion induced by the presence of Bi^{3+} $6s^2$ lone pair electrons, which contributed to the advancement of miniaturised dielectric antennas and microwave filters in mobile communications [19].

To preserve charge neutrality when substituting 12-fold coordinated Ba^{2+}, the replacing $(Bi_{1/2}Na_{1/2})^{2+}$ ions with an average ionic radius of 1.35 Å could be employed to control defect formation and facilitate mass transport during the sintering process. However, research on Bi/Na co-doped BZN perovskite is somewhat limited, with only a few analogous reports available, e.g., $Sr_{1-x}(Na_{1/2}Bi_{1/2})_xBi_2Nb_2O_9$ [17] and $Sr_{1-x}(Na_{1/2}Bi_{1/2})_xTi_{0.99}Mn_{0.01}O_3$ [18]. Furthermore, a thorough understanding of electrical transport characteristics across various temperatures and frequencies is indispensable before any practical application. In this perspective, AC impedance spectroscopy could be employed for analysing relaxation processes, conduction mechanisms and establishing valuable correlations between composition, local structure and electrical processes.

Herein, $(Bi_{1/2}Na_{1/2})^{2+}$ ions are introduced synergically into the A-sites of BZN perovskites for the first time with specific objectives targeted to (i) lower the sintering temperature from 1200 °C to as low as 950 °C, making them suitable for LTCC applications; (ii) study the role of transient phases, e.g., $Na_{0.13}Bi_{1.87}O_{2.87}$ and $ZnNb_2O_6$, in facilitating phase formation and densification at reduced temperatures; (iii) investigate structural and microstructural changes, focusing on the impact of crystallographic structure, grain size and microstructure of BZN perovskites; (iv) optimise the dielectric properties of BZN ceramics, providing valuable insight into the design of functional electronic devices.

2. Experimental

Polycrystalline $(Na_{1/2}Bi_{1/2})_xBa_{1-x}Zn_{1/3}Nb_{2/3}O_3$ ceramics (BNBZN, $x = 0.1$, 0.2, 0.3 and 0.4), abbreviated as BN01, BN02, BN03 and BN04, respectively, were synthesised via solid-state reaction. All high-purity precursors purchased from Alfa Aesar, including $BaCO_3$ (99 %), Na_2CO_3 (99 %), ZnO (99.9 %), Nb_2O_5 (99.9 %) and Bi_2O_3 (99.9 %), were carefully weighed out in accordance with the stoichiometric ratios. Subsequently, these precursors were ground thoroughly in excessive acetone using an agate mortar and pestle. The resulting powders were subjected to calcination at 950 °C for 6 h, followed by an additional grinding process to bring fresh surfaces for reaction. Subsequently, pellets with a diameter of 10 mm and a thickness of 1–2 mm were meticulously formed using a uniaxial hydraulic press under a pressure of 300 MPa. These green pellets were then sintered at temperatures ranging from 950 to 1200 °C for 4 h, employing a heating and cooling rate of 5 °C/min.

The relative density (ρ_r) of densified ceramics was calculated as the ratio of apparent density (ρ_b) to the theoretical density (ρ_t), using the equation below:

$$\rho_r(\%) = \frac{\rho_b}{\rho_t} \times 100 = \frac{\frac{m}{t \times \pi r^2}}{\rho_t} \times 100 \quad (1)$$

where ρ_t, m, r and t denote the theoretical density derived from refinement, the mass, radius and thickness of the pellet, respectively.

The crystallographic phases of the samples were determined using powder X-ray diffraction (XRD-6000, Shimadzu) with Cu Kα radiation ($\lambda = 1.5406$ Å) in the 2θ range of 10–70°. The thermal behaviour of the precursor powders was investigated by thermogravimetry-differential thermal analysis (TG-DTA) using a simultaneous thermal analyser (STA8122, Rigaku) at a heating rate of 10 °C/min in nitrogen, from room temperature to 1000 °C. The surface morphology and chemical composition of the sintered pellets were examined by scanning electron microscopy (JSM-6400, JOEL) equipped with energy-dispersive spectroscopy (EDS) after gold layer sputtering. The vibration characteristics were determined using FT-IR (UATR Spectrum 100, PerkinElmer) and Raman spectroscopy (Alpha 300R, Witec) with an excitation wavelength of 488 nm.

High-resolution transmission electron microscopy (HRTEM) and selected area electron diffraction (SAED) patterns were obtained using a transmission electron microscope (JEM-2100, JEOL). The photoelectron spectra of elements were recorded by an X-ray photoelectron spectrometer (250XI, Thermo). To study the electrical and dielectric properties, the surfaces of sintered pellets were coated with silver paste and cured at 550 °C for 1 h to form electrodes. The dielectric measurements were performed using an AC impedance analyser (1260A, Solartron) over a frequency range of 10 Hz to 1 MHz at temperatures from RT to

750 °C. All data were corrected for the geometry of the samples (thickness/electrode area, - cm^{-1}) and the stray capacitance of the empty jig prior to further analysis using *ZView* software.

3. Results and discussion

$$0.065Na_2CO_3 + 0.935Bi_2O_3 \rightarrow Na_{0.13}Bi_{1.87}O_{2.87} + 0.065CO_2\ T > 400\ ^\circ C \quad (2)$$

$$Zn0 + Nb_2O_5 \rightarrow ZnNb_2O_6\ 700 \leq T \leq 800\ ^\circ C \quad (3)$$

$$0.8BaCO_3 + 0.053Na_{0.13}Bi_{1.87}O_{2.87} + 0.093NaCO_3 + 1\ /\ 3ZnNb_2O_6 \rightarrow Ba_{0.8}Na_{0.1}Bi_{0.1}Zn_{1/3}Nb_{2/3}O_3 + CO_2\ 700 \leq T \leq 900\ ^\circ C \quad (4)$$

3.1. Thermal and structural studies

To establish the optimised calcination temperatures, TG-DSC analysis and qualitative XRD studies were conducted on the BN02 (x = 0.2) precursor mixture. Fig. 1a presents the phase evolution of the BN02 sample following calcination at temperatures up to 900 °C in an air atmosphere. XRD patterns reveal the emergence of a bismuth-rich $Na_{0.13}Bi_{1.87}O_{2.87}$ phase (ICDD# 49–0739) at temperatures exceeding 400 °C, succeeded by the development of the columbite $ZnNb_2O_6$ phase (ICDD# 76–1827) and the BN02 phase at approximately 700 °C. Calcination at 800 °C demonstrates a substantial increase in the proportion of the BN02 phase, potentially attributable to extensive chemical reactions among intermediate phases, as detailed in Eq. (5). Ultimately, calcination at 900 °C and higher temperatures yields a pure cubic BN02 phase, with no detectable secondary phases. The overall phase formation mechanism can be summarised as follows:

On the other hand, TGA data in Fig. 1b exhibits a minor weight loss below 100 °C, corresponding to the removal of moisture or residual acetone solvent. A subsequent mass drop at ~400 °C is supported by an endothermic DSC peak. Such a thermal event could be due to the decomposition of sodium carbonate for the formation of $Na_{0.13}Bi_{1.87}O_{2.87}$ intermediate phase, as shown in Fig. 1a. At ~700 °C, the third weight loss could be attributed to the emergence of intermediate columbite, $ZnNb_2O_6$ and perovskite phase through decomposition of barium carbonate. The last significant weight loss in the range of 800 °C–950 °C highlights that the temperature is sufficient high for a complete chemical reaction for phase pure BN02 perovskite. This mass drop is also accompanied by a rapid decline in DSC heat flow, signifying a reduction in the free energy to form a more stable perovskite. Therefore, the optimum calcination temperature for the synthesis of BNBZN powders was determined to be 950 °C. The total weight loss of 13.28 %, is consistent with the theoretical value of 13.76 %, which reflects the

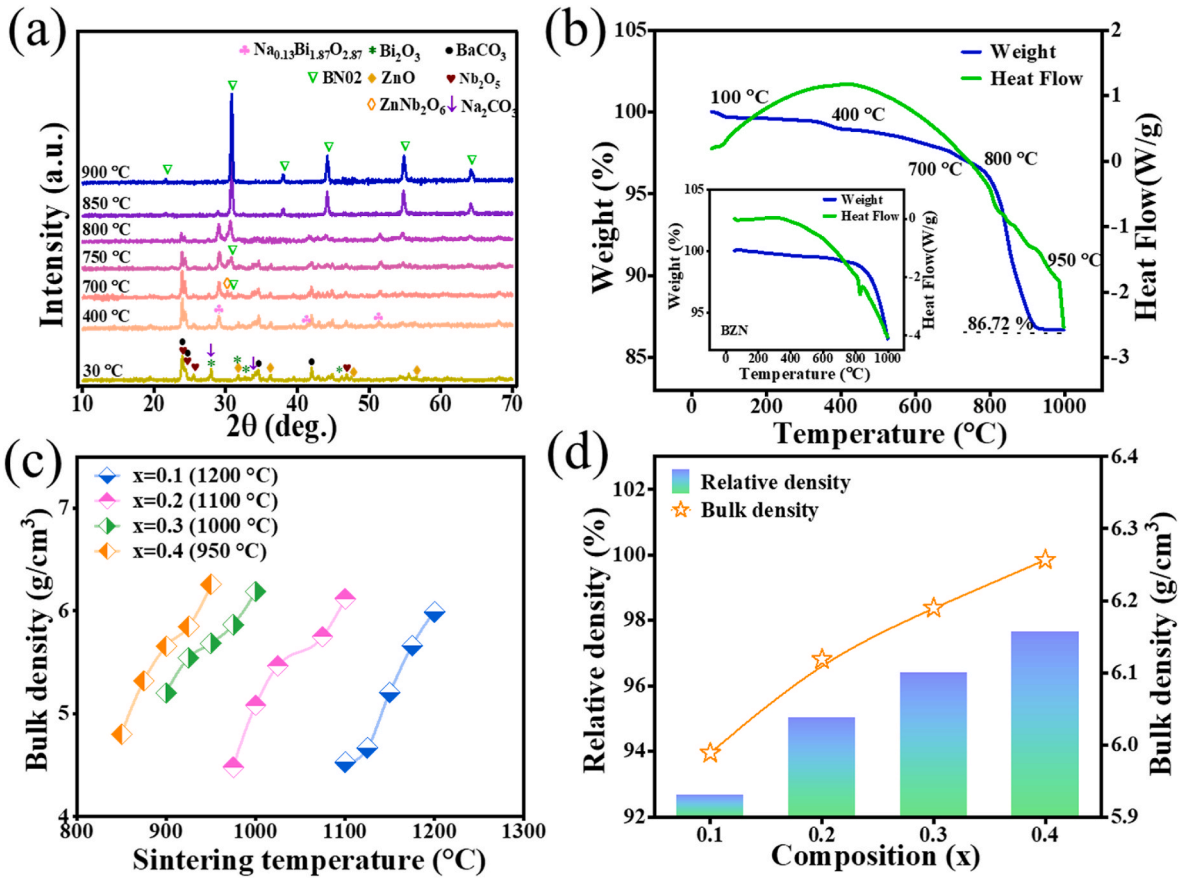

Fig. 1. (a) XRD patterns of the BN02 precursor calcined at various temperatures; (b) TG/DSC thermograms of the BN02 precursor and the related BZN plot shown as an inset; (c) bulk densities of the BNBZN perovskites sintered at different temperatures; (d) bulk and relative densities of BNBZN perovskites sintered at the optimised temperature.

decomposition of metal carbonates.

Interestingly, both TG and DSC thermograms of undoped BZN showcase a continuing decreasing beyond the threshold of measuring temperature, i.e., 1000 °C, as depicted in the insert of Fig. 1b. This provides strong evidence that the formation temperature is significantly reduced by the synergistic doping of $(Na_{1/2}Bi_{1/2})^{2+}$ for Ba^{2+} at the A-site. Notably, the decrease in reaction temperature could be explained by the reduced barrier height of the chemical reaction (E_a) [20]:

$$K = Ae^{-E_a/RT} \tag{5}$$

where K, A, R and T is the chemical reaction rate constant, pre-exponential factor, universal gas constant and reaction temperature in Kelvin, respectively. Assuming a fixed K, a reduced E_a correlates well with a lower T. The comparatively low melting points of Bi_2O_3 (817 °C) and Na_2O (1132 °C), relative to BaO (1923 °C), facilitate their function as flux agents within the reaction, thereby encouraging particle rearrangement and accelerating solid-state diffusion. Furthermore, the smaller ionic radii of Na^+ and Bi^{3+} contribute to enhanced ionic mobility and diffusion rates. The formation of a reactive transient phase ($Na_{0.13}Bi_{1.87}O_{2.87}$) at approximately 400 °C further promotes rapid diffusional activity at lower temperatures. These factors collectively contribute to a reduction in E_a, consequently lowering the formation and sintering temperature.

The variation in bulk density of chemically modified BZN perovskites as a function of sintering temperature is shown in Fig. 1c. All plots depict an obvious increasing density at elevated temperatures wherein the

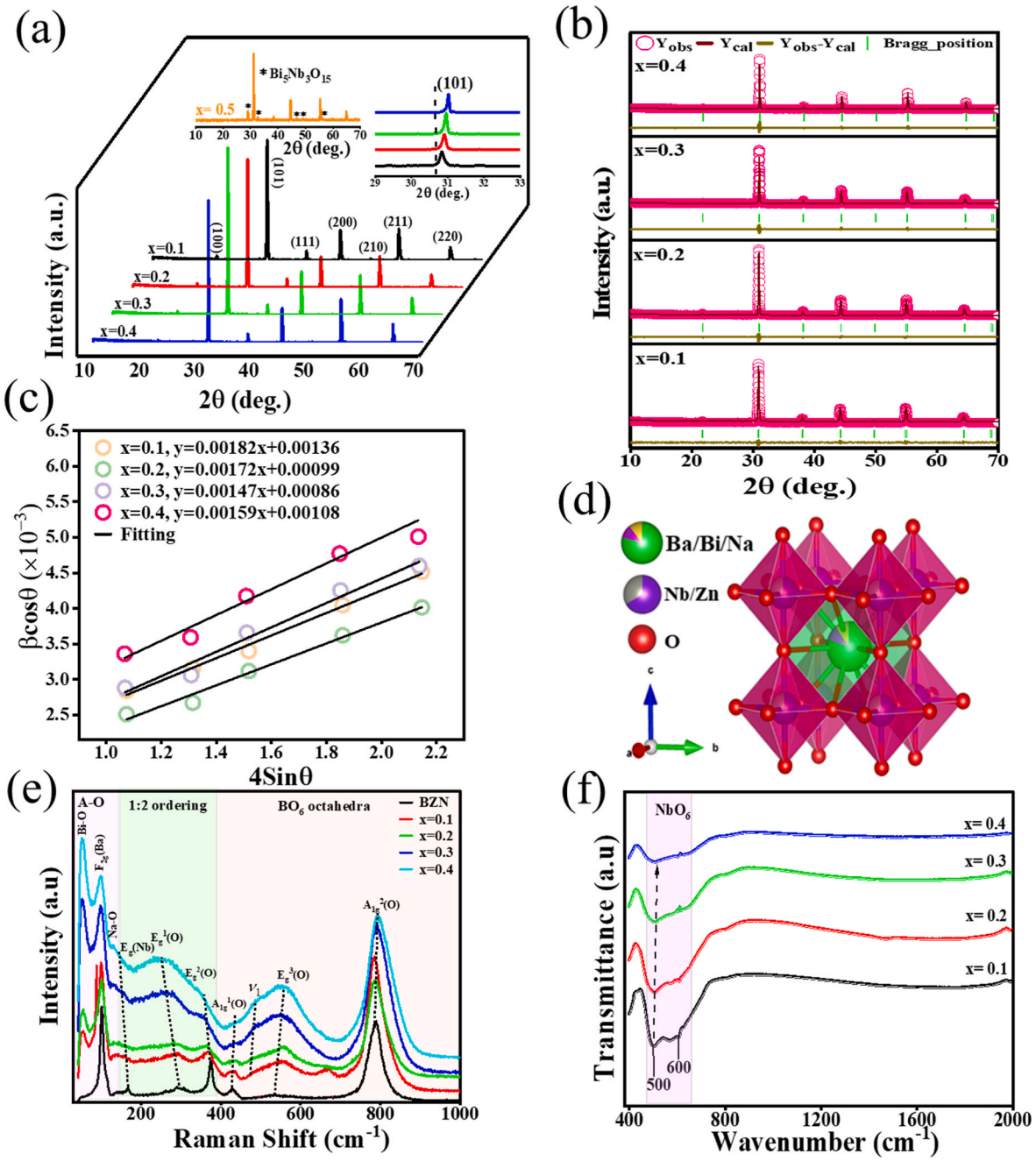

Fig. 2. (a) XRD patterns of BNBZN perovskites with insets showing the XRD pattern for $(Na_{1/2}Bi_{1/2})_{0.5}Ba_{0.5}Zn_{1/3}Nb_{2/3}O_3$ (x = 0.5) ceramics and an enlarged view of the (101) peak; (b) Rietveld-refined XRD patterns of BNBZN perovskites; (c) Williamson-Hall plots; (d) schematic crystal structure of cubic ($Pm\,\bar{3}\,m$) phase of BN02; (e) Raman spectra; (f) FT-IR spectra.

densification process is usually induced by grain growth and boundary migration. However, excessively high sintering temperatures should be avoided to prevent substantial weight loss that may lead to partial melting and compositional non-stoichiometry. The optimal bulk densities, thereby, were achieved at 1200 °C for x = 0.1, 1100 °C for x = 0.2, 1000 °C for x = 0.3 and 950 °C for x = 0.4. Fig. 1d presents the bulk and relative densities of the doped BZN perovskites sintered at their optimal temperatures. It is noteworthy that the increased $(Na_{1/2}Bi_{1/2})^{2+}$ concentration acts as a sintering aid to achieve highly dense microstructure while forming a novel partial subsolidus solution.

The X-ray diffraction (XRD) patterns of the synthesised $(Na_{1/2}Bi_{1/2})_xBa_{1-x}Zn_{1/3}Nb_{2/3}O_3$ perovskites with varying concentrations (x = 0.1, 0.2, 0.3 and 0.4) are presented in Fig. 2a. All the observed diffraction peaks correspond to a cubic perovskite structure with a space group of *Pm* $\bar{3}$ *m* (ICDD# 39–1474). No detectable impurities or secondary phases are discernible within the subsolidus solubility limit ($x \leq 0.4$), indicating the successful incorporation of both Bi^{3+} and Na^{+} into the sublattice of perovskite structure. However, for compositions exceeding this limit, additional diffraction peaks corresponding to the $Bi_5Nb_3O_{15}$ secondary phase (ICDD# 51–1752) are observed (left inset of Fig. 2a). Furthermore, the intense (110) diffraction peak shifts towards a higher angle with increasing $(Na_{1/2}Bi_{1/2})^{2+}$ concentration (right inset of Fig. 2a). This shift is attributed to the smaller average ionic radius of $(Na_{1/2}Bi_{1/2})^{2+}$ (1.35 Å) compared to that of twelve-fold coordinated Ba^{2+} (1.61 Å) [21]. Similar behaviour has been observed for the substitution of Sr^{2+} by $(Na_{1/2}Bi_{1/2})^{2+}$ [22].

For an in-depth study of crystallo-chemical structure, the diffraction patterns of the synthesised ceramics are refined based on a pristine structure model of BZN cubic perovskite using *FULLPROF Rietveld* software (Fig. 2b). A good agreement is observed between the experimental and calculated profiles, with discrepancy R-factors below 10 %, signifying highly coherent results. The refined structural parameters are summarised in Table 1. As x increases, the theoretical density (ρ_t) decreases, reflecting the lower atomic weight of $(Na_{1/2}Bi_{1/2})^{2+}$ than that of Ba^{2+}, notwithstanding the concurrent reduction in unit cell volume. Additionally, the bond lengths at both the A- and B-site decrease progressively with increasing x, consistent with the unit cell contraction suggested by the shift in XRD diffractions. Subsequently, the crystal structure of BN02 was drawn by *VESTA* software, illustrating a network of corner-sharing oxygen octahedra surrounding the twelve-fold coordinate A-site cation (Fig. 2d). Both Zn^{2+}/Nb^{5+} ions are demonstrated to reside at the centre of oxygen octahedra while $Na^{+}/Bi^{3+}/Ba^{2+}$ ions occupy the dodecahedral A-sites, respectively.

To assess the stability of the synthesised perovskites, the Goldschmidt tolerance factor (*t*), based on the chemical formula and ionic radii, was determined using the Shannon and Prewitt's ionic radii for Ba^{2+}, Zn^{2+}, Nb^{5+}, Bi^{3+}, Na^{+} and O^{2-} [22]. As presented in Table 1, the calculated *t* values decreased from 1.016 to 0.982 with higher dopant concentration, suggesting the anticipation of a cubic structure as the *t* value approaches unity [23]. Nonetheless, a potential local structural distortion may arise as the tolerance factor marginally falls below 1, particularly when the doping concentration exceeds 0.2.

Table 1
Refined structural parameters and microstructure parameters of BNBZN perovskites at the optimal sintering temperatures.

x	0.1	0.2	0.3	0.4
$a = b = c$ (Å)	4.09291(6)	4.08706(3)	4.07961(7)	4.07145(9)
V (Å^3)	68.56(7)	68.27(5)	67.90(9)	67.49(10)
ρ_t (g/cm^3)	6.46	6.44	6.42	6.41
ρ_r (%)	92.7	95.0	96.7	97.6
R_p (%)	11.1	7.90	8.93	10.8
R_{wp} (%)	14.1	11.1	11.8	14.9
χ^2	1.92	1.18	1.42	1.88
t	1.016	1.004	0.993	0.982
$D_{W\text{-}H}$ *(nm)*	101.9(45)	140.7(32)	161.6(75)	128.4(87)
D_{Scherr} *(nm)*	41.2(27)	48.08(18)	55.2(56)	45.6(59)
Lattice strain	0.00182(8)	0.00172(10)	0.00147(5)	0.00159(12)
Grain Size (μm)	0.78(14)	2.45(33)	2.29(11)	2.08(20)
A-O (Å)	2.89412(10)	2.88999(22)	2.88472(9)	2.87895(13)
B-O (Å)	2.04645(8)	2.04353(31)	2.03980(28)	2.03573(17)

X-ray peak profile analysis (XPPA) utilising the Debye-Scherrer or Williamson-Hall method serves as an effective means to determine crystallite size [24]. The Debye-Scherrer method operates on the assumption that XRD peak broadening solely originates from variations in crystallite size, as described by:

$$D_{Sch} = \frac{0.9\lambda}{(\beta_{hkl}\cos\theta)} \tag{6}$$

where D_{Sch} denotes the crystallite size (nm), λ is the wavelength of source radiation (λ = 1.5406 Å), β_{hkl} represents the full width at half maximum (FWHM) of the most intense peak in radians and θ is the Bragg's angle. The Williamson-Hall (W-H) approach, another integral breadth technique, considers both crystallite size and lattice strain contributions to the peak broadening [25]:

$$\beta_{hkl}\cos\theta = \frac{0.9\lambda}{D_{WH}} + (4\varepsilon\sin\theta) \tag{7}$$

where ε and D_{WH} denote the lattice strain and average crystallite size, respectively. Five intense diffraction peaks, i.e., (101), (111), (200), (211) and (220), were used for the plot of 4 sinθ *vs* β_{hkl} cosθ (Fig. 2c) wherein the linear fitted slope reveals the internal strain while the y-intercept determines the crystallite size. The calculated crystallite sizes are tabulated in Table 1. Notably, the crystallite sizes obtained from the W-H plot are much larger than those from the Scherrer method, suggesting the emergence of lattice strain and possible lattice distortion.

To further investigate the mesoscopic-scale structure of the BNBZN perovskites, Raman spectroscopy measurements were conducted at room temperature (Fig. 2e). Group theory suggests that an ideal cubic perovskite with a space group of *Pm* $\bar{3}$ *m*, should not exhibit any first-order Raman spectrum. Nevertheless, the presence of discernible Raman-active modes suggests the deviations from ideal symmetry caused by the ion displacements or local symmetry of nano-regions [26]. Within literature, the Raman spectra of complex perovskites can be categorised into three main bands [27,28]: (i) the A-site cationic vibrations (50-200 cm^{-1}); (ii) the B-site cation ordering band (200-400 cm^{-1}) and (iii) the BO_6 octahedral vibrations (400-900 cm^{-1}).

On this basis, the first low-frequency mode at ~52 cm^{-1} is assigned to the Bi-O vibration due to the relatively higher mass of Bi^{3+} (m = 208.98 g/mol) compared to Na^{+} (m = 23.00 g/mol) and Ba^{2+} (m = 137.33 g/mol). This mode is highly sensitive to any A-site cation off-centre and Bi^{3+} possesses a greater tendency towards off-centre from the twelve surrounding O^{2-} anions than Na^{+} [29]. The active mode at ~98 cm^{-1}, commonly observed in the Ba-based complex perovskites, is assigned to the F_{2g} (Ba) mode, which is associated with the lattice vibration of Ba^{2+} relative to the oxygen octahedra [30]. The last peak in the A-O vibration band is ascribed to Na-O vibrations (~131 cm^{-1}).

In the mid-frequency range (200–400 cm^{-1}), the modes located at 165 cm^{-1} [E_g(Nb)], 290 cm^{-1} [E_g^1(O)] and 374 cm^{-1} [E_g^2(O)] are typically indicative of the localised 1:2 ordering of complex perovskites [31]. As x increases to 0.2, the decreasing intensity of these modes suggests a weakened B-site chemical order. Notably, a red shift is observed for these modes, contradicting the prediction that Raman modes should exhibit a blue shift as both the bond length and molecular mass decrease with increasing substitution concentration (x). This behaviour could be explained by a reduction in the force constant *k*, induced by the decreasing ordering degree, i.e., weakened interactions among B-site cations, resulting in the observed red shift. Moreover, these broadened peaks suggest increasing disorder within the matrix, which is probably attributed to the random occupancy of Na^{+} and Bi^{3+} at the A-site [32].

In the high frequency region, modes A_{1g}^1 (O) (~427 cm^{-1}), E_g^3(O)

(~523 cm^{-1}) and A_{1g}^2 (O) (~792 cm^{-1}), are all resulting from oxygen octahedron vibrations [33]. An additional peak at ~473 cm^{-1} (ν_1) for x = 0.1, could be attributed to the strengthened oxygen octahedra tilting and/or local lattice deformation [6,34]. Such phenomenon is indicated by the decreasing tolerance factor (*t*) and average ionic radii at the A-site. The most intense A_{1g}^2 (O) vibration mode, corresponding to the stretching of oxygen octahedron along the c-axis, serves as an indicator of B-site cation ordering [27]. A broader A_{1g}^2 (O) mode with increasing x qualitatively indicates enhanced phonon interference and thus a decreased degree of ordering, corroborating the analysis of the B-site cation ordering band.

The FT-IR spectra of BNBZN perovskites, as illustrated in Fig. 2f, exhibit a pattern similar to that of undoped BZN [35], as measured at room temperature within the 400–2000 cm^{-1} range. The characteristic absorption bands below 800 cm^{-1} correspond to the symmetric stretching mode of the NbO_6-octahedra in the perovskite structure [36]. As the x value increases, a blue shift in this octahedral band is observed, consistent with the Raman results. Simultaneously, the gradual decrease in the band's intensity implies reduced coherence of Nb-O vibrations and a lower ordering degree arising from the heterogeneous local environment induced by mixed occupancy at the A-site [37]. Furthermore, a slight dip observed in the lower frequency region (400-420 cm^{-1}) is attributed to Nb-O bending vibrations.

3.2. Microstructural characterisation

The SEM micrographs of all the prepared BNBZN perovskites sintered at their optimal temperatures are shown in Fig. 3a–d. All compositions exhibit a dense microstructure with well-defined grains ranging from ~0.8 to 2.5 μm. The obtained average grain sizes significantly exceed the aforementioned crystallite sizes, indicating the polycrystalline nature of these perovskites. At low doping concentrations ($x \leq 0.2$), the doping elements facilitate grain growth by acting as sintering aids. Notably, the smaller ionic radii of Na^+ and Bi^{3+} contribute to a higher ionic mobility and rapid diffusion rate, enhancing grain boundary mobility during sintering. However, excessive dopant ($x > 0.2$) can lead to a smaller average grain size, associated with the reduced surface anisotropy energy, potentially due to hindered ionic diffusion [30]. Furthermore, all the BNBZN perovskites exhibit larger grain sizes and a denser microstructure than the undoped BZN [35]. Such a phenomenon can be attributed to the lower melting points of Bi_2O_3 (817 °C) and Na_2O (1132 °C) compared to BaO (1923 °C), which act as flux agents during sintering. Similar behaviour has been reported for $Sr_{1-x}(K_{1/2}Bi_{1/2})_xBi_2Nb_2O_9$ [38].

The elemental distribution analysis for BN02 was conducted using EDS. As displayed in Fig. 3e, the characteristic peaks of Ba, Bi, Na, Zn, Nb and O constituent ions in the EDS spectrum are observed, confirming the successful substitution of $(Na_{1/2}Bi_{1/2})^{2+}$ for Ba at the A-sites. The atomic and weight percentages show that the experimental values are in accordance with the expected stoichiometry with negligible Bi losses (Fig. 3f).

Meanwhile, the microstructure of BN02 ceramics was further investigated using Transmission Electron Microscopy (TEM). The Selected Area Electron Diffraction (SAED) pattern exhibited distinct diffraction spots, corresponding to the $[\bar{1}32]$ zone axis of a cubic structure (Fig. 3g). The High-Resolution Transmission Electron Microscopy

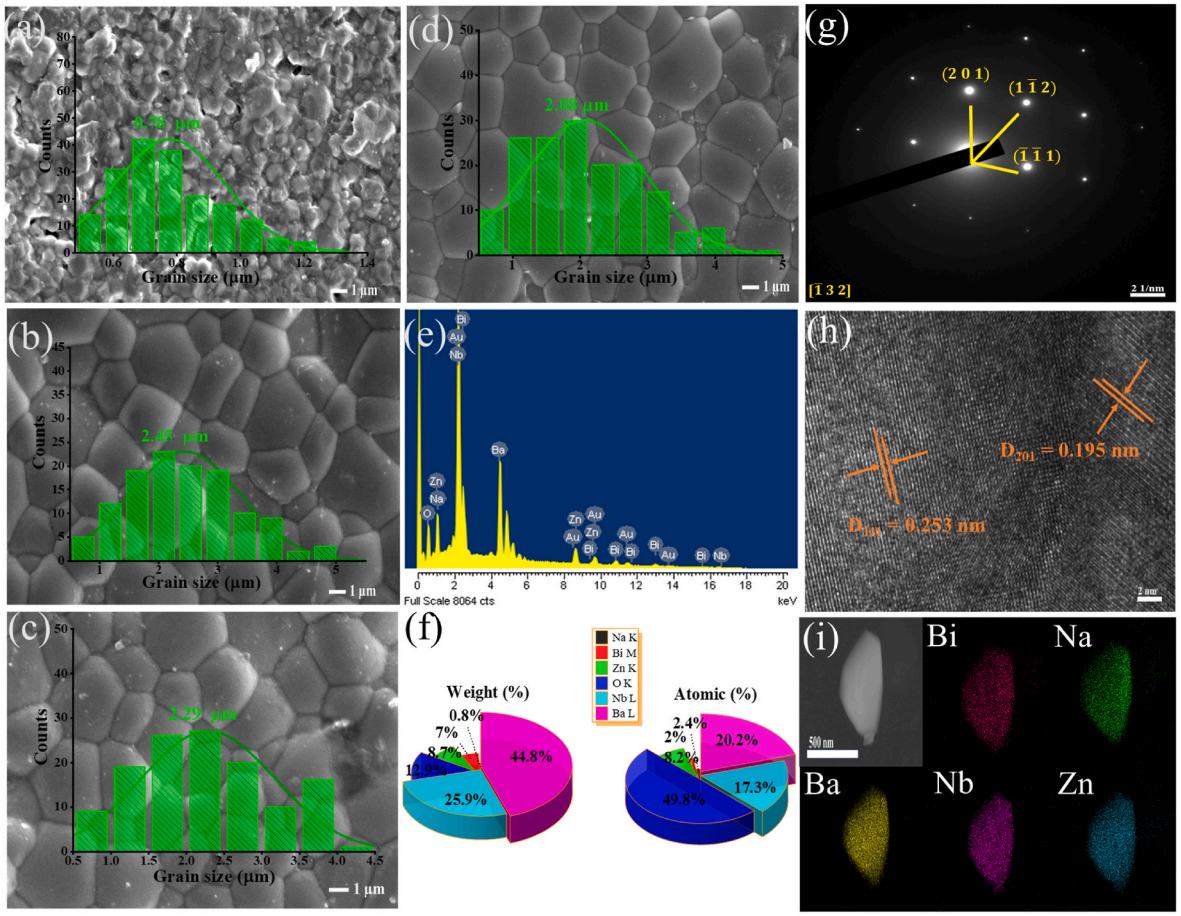

Fig. 3. SEM images of BNBZN perovskites sintered at their optimal temperatures: (a) x = 0.1, (b) x = 0.2, (c) x = 0.3, and (d) x = 0.4, with corresponding grain size distribution histograms shown in the insets; (e) EDS spectrum of BN02 (x = 0.2) and (f) corresponding atomic and weight fractions; TEM analysis of BN02: (g) SAED pattern, (h) HRTEM image; (i) TEM-EDS elemental mapping.

(HRTEM) image (Fig. 3h) revealed lattice fringes with interplanar spacings of 0.253 and 0.195 nm, corresponding to the (111) and (201) crystal planes of the cubic-structured BN02, respectively. Furthermore, the TEM Energy Dispersive X-ray Spectroscopy (EDS) mapping also confirmed a uniform distribution of lattice cations without any aggregation or segregation, indicating a good chemical homogeneity of the material (Fig. 3i).

X-ray photoelectron spectroscopy (XPS) analysis was conducted to investigate the oxidation states and chemical environment of the constituent elements. The XPS survey spectrum of BN02 ceramics, calibrated to the C 1s peak at 284.8 eV, confirmed the presence of Ba^{2+}, Zn^{2+}, Nb^{5+}, Bi^{3+}, Na^{+} and O^{2-} without any detectable impurities. Again, this indicates successful substitution of Ba^{2+} by $(Na_{1/2}Bi_{1/2})^{2+}$ ions. The deconvoluted XPS spectra using a Lorentzian function for BN02 are presented in Fig. 4b–g. As displayed in Fig. 4b, the peaks ascribed to Ba^{2+} ions, namely Ba $3d_{5/2}$ (779.56 eV) and $3d_{3/2}$ (794.80 eV), are clearly visible [39]. The presence of Nb^{5+} is manifested by the binding energies of the $3d_{3/2}$ level (209.48 eV) and $3d_{5/2}$ level (206.74 eV), with a spin-orbit splitting of 2.74 eV (Fig. 4c) [40]. Two peaks for the Zn 2p state, Zn $2p_{3/2}$ (1021.87 eV) and Zn $2p_{1/2}$ (1044.90 eV), are attributed to Zn^{2+} ions (Fig. 4d) [41]. In addition, the core level spectra of Bi^{3+} show two peaks centred at 159.11 eV and 164.44 eV for $4f_{7/2}$ and $4f_{5/2}$ states, respectively, with an area ratio of ~ 4:3 between the $4f_{7/2}$ and $4f_{5/2}$ peaks (Fig. 4e) [42]. As shown in Fig. 4f, Na^{+} is manifested by a single peak at 1072.29 eV for Na 1s. Interestingly, the deconvoluted spectra for Bi^{3+} and Na^{+} closely resemble those reported for $(Na_{1/2}Bi_{1/2})TiO_3$ perovskites [39,42], further confirming the successful substitution of A-site cations. Fig. 4g shows the O 1s region, deconvoluted into two peaks at 529.84 eV and 531.83 eV, corresponding to lattice oxygen species (O_{lat}) and adsorbed oxygen (O_{ads}), respectively [43]. The oxygen vacancies (OVs) in BN02 perovskites are closely associated with the area of the O_{ads} peak, and the deconvolution area ratio of O_{ads} to O_{lat} is 0.54, lower than that of pure BZN (0.61), signifying a reduction in OVs after the A-site doping.

The observed reduction in oxygen vacancies (OVs) may be linked to the lower sintering temperature of BN02 compared to undoped BZN. The generation of OVs in perovskites is typically associated with oxygen depletion during high-temperature sintering under reduced oxygen partial pressure, e.g., in air or vacuum environment [44]. Furthermore, the decreased sintering temperature could potentially limit the volatilisation of Bi_2O_3 and Na_2O, which often leads to A-site vacancies and the subsequent formation of oxygen vacancies to preserve charge neutrality. Moreover, the refined shorter and stronger average A-O bond length of BN02 also potentially leads to this reduced OVs due to the strengthened binding force of oxygen ions [45].

3.3. Dielectric studies

Both ε' and tan δ at ambient temperature (~25 °C) exhibit a decreasing trend with increasing frequency, reaching a plateau in the high-frequency region (Fig. 5a and b). As illustrated in the inset of Fig. 5a, ε' at 1 MHz characterising bulk response exhibits a rising trend as the $(Na_{1/2}Bi_{1/2})^{2+}$ concentration increases, which is higher in all cases compared to undoped BZN. This observation is consistent with the reported $Sr_{1-x}(Na_{0.5}Bi_{0.5})_xTi_{0.99}Mn_{0.01}O_3$ ($0 \le x \le 0.02$) thin films and $Sr_{1-x}(K_{0.5}Bi_{0.5})_xBi_2Nb_2O_9$ ($0.02 \le x \le 0.10$) bulk ceramics [18,38]. The Clausius-Mossotti equation defines the relationship between microscopic ionic polarisability ($\alpha_{theo.}$) and the macroscopic dielectric constant [46]:

$$\varepsilon' = \frac{3 + 8\pi\alpha_{theo}/V_m}{3 - 4\pi\alpha_{theo}/V_m} \tag{8}$$

where $V_{m.}$ represents the molar volume. Notably, ε' is proportional to polarisability density ($\alpha_{theo.}/V_m$) and $\alpha_{theo.}$ can be mathematically expressed by the Shannon additive rule [11]:

$$\alpha_{theo.} = (1-x)\alpha(Ba^{2+}) + x\alpha\left[(Na_{1/2}Bi_{1/2})^{2+}\right] + \alpha\left[(Zn_{1/3}Nb_{2/3})^{4+}\right] + 3\alpha(O^{2-}) \tag{9}$$

where $\alpha(Ba^{2+})$ = 6.40 Å^3, $\alpha[(Na_{1/2}Bi_{1/2})^{2+}]$ = 3.96 Å^3, $\alpha[(Zn_{1/3}Nb_{2/3})^{4+}]$ = 3.33 Å^3 and $\alpha(O^{2-})$ = 2.01 Å^3 [47]. The calculated $\alpha_{theo.}$ and $\alpha_{theo.}/V_m$ values are presented in Table 2.

The $\alpha_{theo.}/V_m$ appears to be independent of doping concentration, indicating that other factors, e.g., sintering temperature, microstructural defect, grain size, cation ordering and contributing dopant species, should be considered to account for the observed increasing ε'. A comparative summary of the dielectric properties from this work and the related studies is included in Table 3. Notably, the active $6s^2$ lone-pair electrons of the Bi^{3+} cation may induce dipole polarisation through off-centre displacements and this results in the increase in ε' with x. In addition, a smaller divalent pseudo-cation $(Na_{1/2}Bi_{1/2})^{2+}$ into the Ba^{2+} site may enhance the rotational freedom of the oxygen octahedra, thereby enhancing the dielectric response [38].

The inset of Fig. 5b illustrates the variation in the tan δ at 1 MHz with composition. Initially, tan δ decreases from 0.058 at x = 0.1 to 0.009 at x = 0.2. Subsequently, it increases with higher dopant concentration. The optimal tan δ achieved at x = 0.2 can be attributed to the relatively larger grain size of BN02 compared to other compositions. This signifies fewer grain boundaries where impurities and defects tend to accumulate. Furthermore, tan δ can be influenced by the internal cause of lattice vibrations, which can be defined by the intrinsic packing fraction (P.F.) [48]:

$$Packing\ fraction = \frac{4\pi}{3} \times \frac{(1-x)R_{Ba}^3 + \frac{1}{3}R_{Zn}^3 + \frac{2}{3}R_{Nb}^3 + xR_{Bi/Na}^3 + 3R_O^3}{V_m} \times Z \tag{10}$$

where Z (=1) represents the unit formula of perovskite structure. In Table 2, there is a gradual decline in P.F. as x increases. This accounts for the upward trend of tan δ, which corresponds to loosely packed crystal structures that contribute to potential scattering losses and/or defect-induced energy dissipation [49]. Additionally, the B-site cation ordering can play a role in energy dissipation for complex perovskites. The increment of the FWHM of the A_{1g}(O) Raman mode suggests weakened ordering and thus increased tan δ [50].

3.4. Impedance spectroscopy

Typical complex impedance plane (Z*) plots for BN02 are shown in Fig. 6a, and it is noteworthy that the other compositions exhibited similar characteristics. A semi-circular arc only becomes visible at ~550 °C due to the electrically insulating nature of the samples. At higher frequencies, a single suppressed semicircle emerges from the origin, decreasing in diameter as temperature increases with no sign of any low frequency spike. This behaviour indicates Negative Temperature Coefficient of Resistance (NTCR) behaviour based on grain (bulk) effects. To further investigate the correlation between x, microstructure and the conduction properties, all data were modelled on a single parallel RC equivalent circuit, consisting of a capacitor (C) and a resistor (R). The use of a parallel RC element instead of an R-CPE (Constant Phase Element) model was based on the fact that the observed depression of the semicircle was subtle and could be satisfactorily fitted to obtain the resistances R [51]. The Arrhenius-type plots of ln (R) for all samples are shown in Fig. 6b. By extrapolating the linear fit, the activation energy for the bulk conduction was ~1.22, 2.01, 1.79 and 1.29 eV for BN01, BN02, BN03 and BN04, respectively, which reveals x = 0.2 to have the highest insulation resistance because of its higher energy barrier for the charge carrier movement and/or the reduced oxygen vacancies concentration, as evidenced by XPS analysis. Interestingly, the variation of activation energy with x shows an inverse relationship with that of tan δ, suggesting that conductive loss may also contribute to the

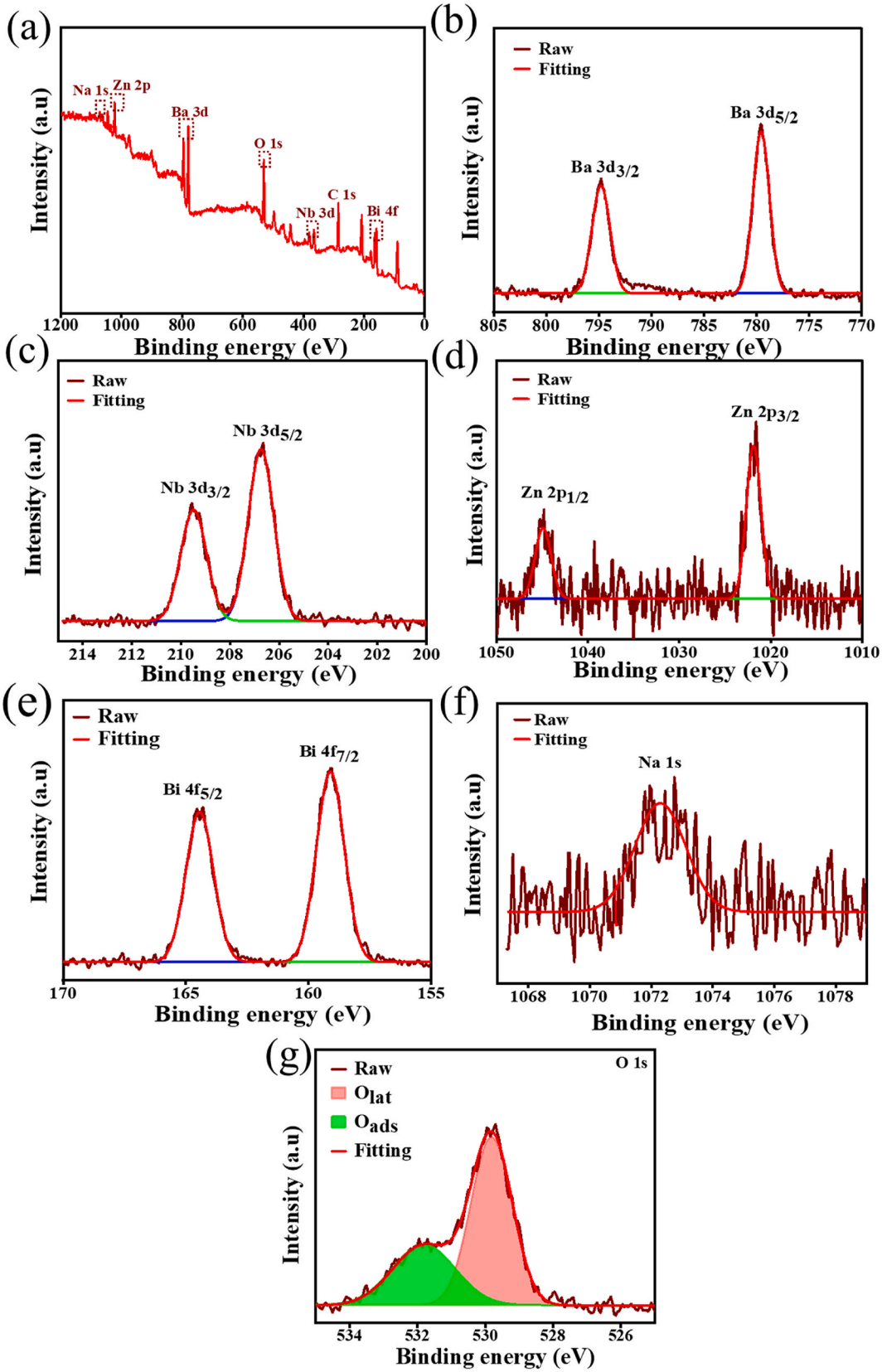

Fig. 4. XPS spectra of BN02 perovskite: (a) Full survey; (b) Ba 3d; (c) Nb 3d; (d) Zn 2p; (e) Bi 4f; (f) Na 1s; (g) O 1s.

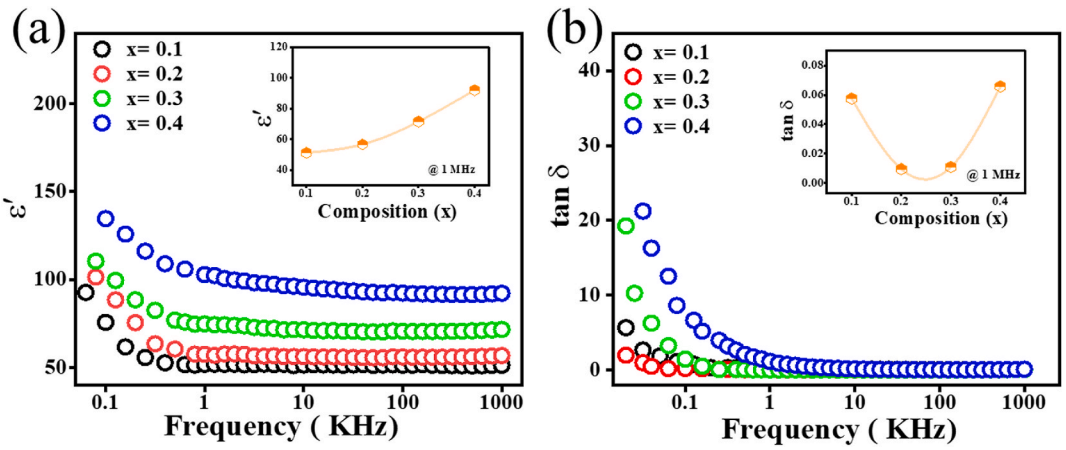

Fig. 5. Frequency-dependent dielectric properties of BNBZN perovskites at 30 °C: (a) ε' with inset of ε' vs. composition (x); (b) tan δ with inset of tan δ vs. composition (x).

Table 2
Calculated dielectric properties, $\alpha_{theo.}$, $\alpha_{theo.}/V_m$ and P.F. values of the BNBZN perovskites.

x	ε' (1 MHz)	tan $\delta \times 10^{-2}$ (1 MHz)	P. F. (%)	$\alpha_{theo.}$	α_{theo}/V_m
0.1	51.2	5.8	76.6	15.76	0.23
0.2	56.8	0.9	75.9	15.52	0.23
0.3	71.6	1.1	75.3	15.27	0.22
0.4	92.1	6.6	74.7	15.03	0.22

Table 3
Sintering temperature and corresponding dielectric properties of BZN-based ceramics.

Material	Temperature	ε'	tan δ/$Q \times f$	Ref.
$0.7ZnNb_2O_6$–$0.3Ba(Zn_{1/3}Nb_{2/3})O_3$	1200 °C/4 h	31	39,611 (GHz)	[5]
$(Ba_{1-x}Sr_x)(Zn_{1/3}Nb_{2/3})O_3$	1400 °C/3 h	42	11,550 (GHz)	[6]
BZN+15 mol % $BaLiF_3$	1150 °C/2 h	48	Not Available	[7]
$Ba_{0.99}Zn_{1/3}Nb_{2/3}O_3$	1450 °C/4 h	39	66,532 (GHz)	[8]
$Ba(Zn_{1/3}Nb_{2/3})_{0.98}Zn_{0.02}O_3$	1500 °C/2 h	–	0.0005 (1 MHz)	[9]
BZN + 5 mol% B_2O_3	900 °C/2 h	32	3500 (GHz)	[10]
$Ca_{0.9}Ba_{0.1}(Zn_{1/3}Nb_{2/3})O_3$	1200 °C/3 h	36	16,170 (GHz)	[14]
$La_{0.1}Ba_{0.9}(Zn_{1/3}Nb_{2/3})O_3$	1350 °C/4 h	35	0.005 (1 MHz)	[15]
BN02	1100 °C/4 h	56	0.0096 (1 MHz)	Current Work
BN04	950 °C/4 h	92	0.066 (1 MHz)	Current Work

dielectric loss.

To probe the electrical homogeneity of the ceramics, combined -Z″, M″ spectroscopic plots were inspected. The M″ spectra, highlighting the effect of small capacitance, serve as an indicator of a grain-dominated electrical process. There is good overlap between the -Z″ and M″ Debye-type peaks for BN02 at 550 and 750 °C (Fig. 6c), which confirms the Z* plots are dominated by a bulk (grain) response. Fig. 6d illustrates the variation of M″ plots for all x at 750 °C. It is evident that a single relaxation peak appears in the high-frequency region, confirming the grain-dominated electrical process across the compositions. The progressive reduction in M''_{max} indicates that the addition of $(Na_{1/2}Bi_{1/2})^{2+}$ significantly enhances the capacitance of undoped BZN, which is consistent with the aforementioned increased ε' from the dielectric measurements in Fig. 5a. Notably, the relaxation frequency (f_{max}) exhibits a similar non-monotonic variation trend to that of tan δ in Fig. 5b, initially decreasing up to x = 0.2 before increasing with higher dopant concentration. This behaviour can be primarily attributed to the introduction of a small amount of Na^+/Bi^{3+} into the BZN matrix, which increases the grain impedance and consequently slows down the relaxation process. On the contrary, higher doping concentration facilitates enhanced charge carrier movement due to lattice defects that possibly originate from volatilisation, leading to greater tan δ [52]. Further studies are required to elucidate the bulk conduction mechanism(s) in these materials.

Although no low-frequency electrode spike was observed in the IS data, empirically suggesting that the dominant conducting species are electrons [53], there may be some ionic conduction associated with OVs induced during the firing of BNBZN perovskites. As is well known, the presence of OVs in perovskites can exist in different charge states, i.e., single ionised oxygen vacancies $(V_o^{\cdot})$ and/or doubly ionised oxygen vacancies $(V_o^{\cdot\cdot})$, expressed by Kröger-Vink notation [54]:

$$O_o^x \rightarrow V_o^{\cdot} + e + 1/2O_2 \quad (11)$$

$$V_o^{\cdot} \rightarrow V_o^{\cdot\cdot} + e \quad (12)$$

Considering that the activation energy for bulk conduction in this study lies in the range of (1.2–2.01 eV), comparable to the reported activation energies (1.2–1.6 eV) for ionic conduction by $V_o^{\cdot\cdot}$ in perovskite-type oxides [55,56], it is reasonable to reckon that the conduction mechanism may involve a mixed contribution from both electronic and oxygen-vacancy-mediated ionic transport.

4. Conclusion

In this study, the novel Bi and Na co-doped $(Na_{1/2}Bi_{1/2})_xBa_{1-x}Zn_{1/3}Nb_{2/3}O_3$ (x = 0.1, 0.2, 0.3 and 0.4) perovskites were successfully synthesised using solid-state reaction. These chemically modified perovskites exhibited dense microstructure and well-packed grains with an average size between ~0.8 and 2.5 μm, resulting in high relative density ($\rho_r > 92$ %). The introduction of $(Na_{1/2}Bi_{1/2})^{2+}$ enhances densification, thereby reducing the sintering temperature significantly from 1200 °C to 950 °C. Dielectric studies revealed increased ε' and tan δ with increasing x, primarily due to enhanced dipole polarisation and the synergistic effects of grain size, packing fraction, cation ordering and activation energy. Notably, the composition, x = 0.2 sintered at 1100 °C for 4 h, exhibits enhanced ambient relative permittivity ($\varepsilon' \sim 57$) compared to undoped BZN and has the lowest dielectric loss (tan δ ~ 0.0096 at 1 MHz), whereas x = 0.4 displays the highest ε' (~92) and dielectric loss (>0.06) along with the lowest sintering temperature of 950 °C. All

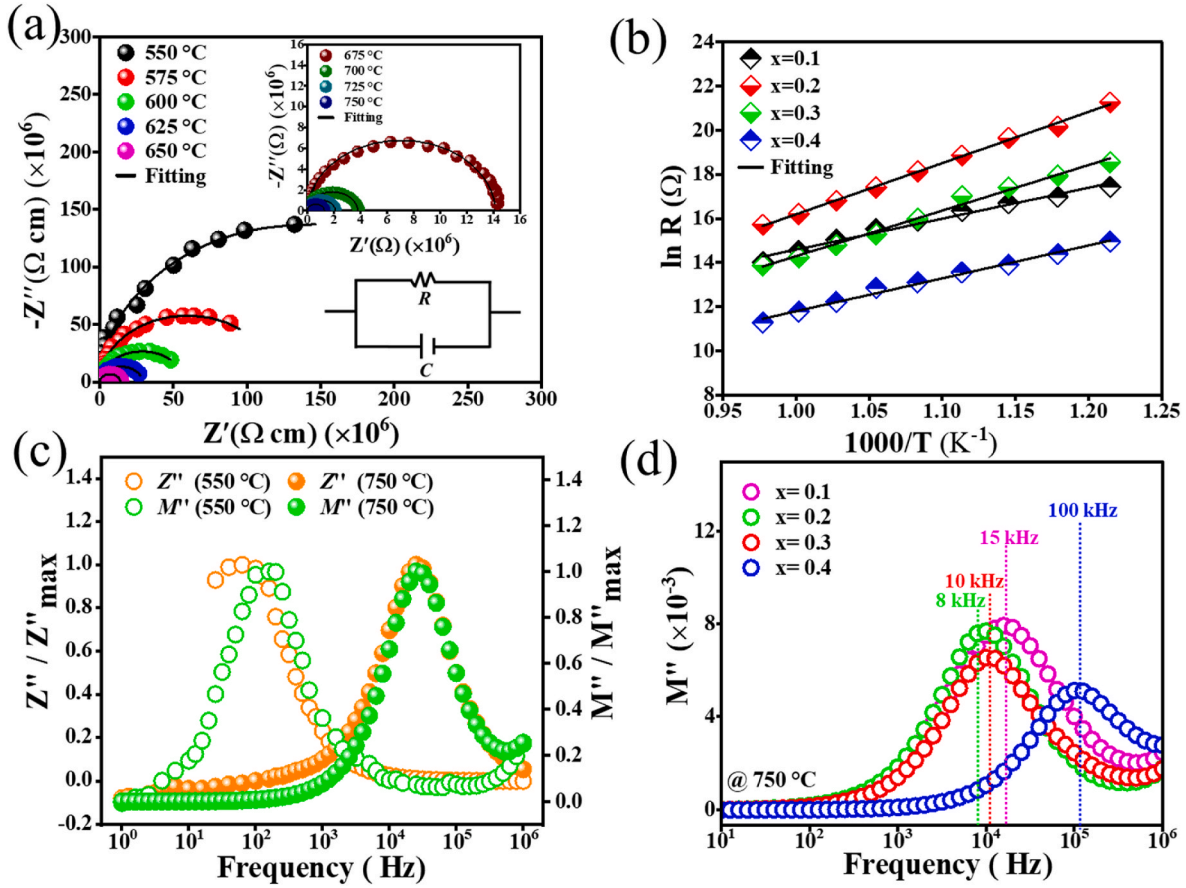

Fig. 6. (a) Fitted Cole-Cole plots of BN02 perovskite, with the equivalent circuit *RC* shown in the inset; (b) ln *R* as a function of 1000/*T*; (c) frequency dependence of normalised peaks, M''/M''_{max} and Z''/Z''_{max} for BN02 perovskite at varying temperatures; (d) M'' vs. frequency for BNBZN perovskites.

compositions exhibit modest bulk conduction at elevated temperatures (>500 °C) with an associated activation energy in the range of ~1.0–2.0 eV, showing these materials to have good insulation resistance properties at lower temperatures. These findings indicate that further optimisation of NBBZN perovskites to reduce the dielectric loss of ceramics sintered below 1000 °C could yield dielectrics suitable for integration with Ag or Au electrodes through LTCC processing.

CRediT authorship contribution statement

Y. Feng: Writing – original draft, Methodology, Investigation, Formal analysis. **A.T.Z. Lim:** Formal analysis, Validation, Visualization. **M. Lu:** Methodology, Investigation, Formal analysis. **J. Sun:** Validation, Software, Data curation. **K.Y. Chan:** Validation, Software, Data curation. **S. Ghotekar:** Visualization, Validation, Methodology. **D. Zhou:** Validation, Software, Methodology. **D.C. Sinclair:** Writing – review & editing, Validation, Funding acquisition, Data curation. **K.B. Tan:** Writing – review & editing, Supervision, Resources, Project administration, Funding acquisition, Conceptualization.

Declaration of competing interest

The authors declare that they have no known competing financial interests or personal relationships that could have appeared to influence the work reported in this paper.

Acknowledgements

The financial supports from the Ministry of Higher Education, Malaysia via the Fundamental Research Grant Scheme (FRGS/1/2020/STG05/UPM/02/2) and Putra Graduates Initiative Grant (GP-IPS-2023/9773100) are gratefully acknowledged. The authors are also grateful for the International Research Collaborations Grant (C23-3428533935) support from the Royal Society of Chemistry, United Kingdom.

References

[1] W. Bai, Y. Zhou, M. Xiao, L. Xu, H. Xiao, Y. Tong, C. He, J. Pang, Q. Xie, C. Yang, Effects of Cu ion implantation on the microstructure, dielectric and impedance properties of $SrTiO_3$ ceramics prepared by reduction-reoxidation method, Ceram. Int. 50 (22) (2024) 46279–46287, https://doi.org/10.1016/j.ceramint.2024.08.470.

[2] L. Chen, S. Deng, H. Liu, J. Wu, H. Qi, J. Chen, Giant energy-storage density with ultrahigh efficiency in lead-free relaxors via high-entropy design, Nat. Commun. 13 (1) (2022) 3089, https://doi.org/10.1038/s41467-022-30821-7.

[3] Z. Lou, X. Xu, P. Zhang, L. Gong, Q. Chen, J. Xu, A. Rydosz, F. Gao, Microstructure and dielectric properties of high-entropy $Sr_{0.9}La_{0.1}MeO_3$ (me: zr, Sn, Ti, Hf, Mn, Nb) perovskite ceramics, J. Mater. Res. Technol. 21 (2022) 850–858, https://doi.org/10.1016/j.jmrt.2022.09.081.

[4] L. Dupont, L. Chai, P. Davies, A-and B-site order in $(Na_{1/2}La_{1/2})(Mg_{1/3}Ta_{2/3})O_3$ perovskites, MRS Proc. 547 (1998) 93, https://doi.org/10.1557/PROC-547-93.

[5] W. Xie, Q. Jiang, Q. Cao, H. Zhou, L. Ren, X. Luo, Microwave dielectric properties of $(1-x)ZnNb_2O_6$–$xBa(Zn_{1/3}Nb_{2/3})O_3$ compound ceramic with near zero temperature coefficient, J. Mater. Sci. Mater. Electron. 29 (3) (2018) 2170–2174, https://doi.org/10.1007/s10854-017-8129-2.

[6] F. Shi, H. Dong, Correlation of crystal structure, dielectric properties and lattice vibration spectra of $(Ba_{1-x}Sr_x)(Zn_{1/3}Nb_{2/3})O_3$ solid solutions, Dalton Trans. 40 (25) (2011) 6659–6667, https://doi.org/10.1039/c0dt01507e.

[7] F. Roulland, R. Terras, G. Allainmat, M. Pollet, S. Marinel, Lowering of $BaB'_{1/3}B''_{2/3}O_3$ complex perovskite sintering temperature by lithium salt additions, J. Eur. Ceram. Soc. 24 (6) (2004) 1019–1023, https://doi.org/10.1016/s0955-2219(03)00553-3.

[8] J. Wang, W. Lu, W. Lei, Effects of Ba deficiency on ion ordering, grain growth, and microwave dielectric properties of $Ba_{1-x}Zn_{1/3}Nb_{2/3}O_3$ ceramics, Jpn. J. Appl. Phys. 51 (4R) (2012) 041501, https://doi.org/10.1143/jjap.51.041501.

[9] J. Li, C. Xing, H. Qiao, H. Chen, J. Yang, H. Dong, F. Shi, Crystal structure characteristics, dielectric loss, and vibrational spectra of Zn-rich non-

stoichiometric Ba[$(Zn_{1/3}Nb_{2/3})_{1-x}Zn_x$]$O_3$ ceramics, Mater. Res. Express 4 (7) (2017) 075910, https://doi.org/10.1088/2053-1591/aa7bfc.
[10] M.-H. Kim, Y.-H. Jeong, S. Nahm, H.-T. Kim, H.-J. Lee, Effect of B_2O_3 and CuO additives on the sintering temperature and microwave dielectric properties of Ba$(Zn_{1/3}Nb_{2/3})O_3$ ceramics, J. Eur. Ceram. Soc. 26 (11) (2006) 2139–2142, https://doi.org/10.1016/j.jeurceramsoc.20-05.09.072.
[11] B. Zhang, L. Li, W. Luo, Oxygen vacancy regulation and its high frequency response mechanism in microwave ceramics, J. Mater. Chem. C 6 (41) (2018) 11023–11034, https://doi.org/10.1039/c8tc03936d.
[12] H. Li, F. Liu, L. Cheng, J. Huang, S. Liu, Microstructure and microwave properties of complex perovskite-structured Ba$(Zn_{1/3}Nb_{2/3})O_3$ ceramics and dielectric resonator antenna by digital light processing technology, J. Eur. Ceram. Soc. 45 (13) (2025) 117492, https://doi.org/10.1016/j.jeurceramsoc.2025.117492.
[13] H. Li, F. Liu, K.C. Chang, X. Lin, S. Liu, Accelerating B site cation ordering disordering transition and improving dielectric properties of Ba(Co, Zn)$_{1/3}Nb_{2/3}O_3$ complex perovskite microwave ceramics by CuO doping, J. Am. Ceram. Soc. 107 (9) (2024) 6152–6163, https://doi.org/10.2139/ssrn.4661426.
[14] D. Liu, X.M. Chen, X. Hu, Microwave dielectric ceramics in $(Ca_{1-x}Ba_x)(Zn_{1/3}Nb_{2/3})O_3$ system, Mater. Lett. 61 (4) (2007) 1166–1169, https://doi.org/10.1016/j.matlet.2006.06.077.
[15] A.F. Qasrawi, E.İ. Sahin, T.Y. Abed, M. Emek, Structural and dielectric properties of $Ba_{1-x}La_x(Zn_{1/3}Nb_{2/3})O_3$ solid solutions, Phys. Status Solidi (B) 258 (3) (2021) 2000419, https://doi.org/10.1002/pssb.202000419.
[16] H.U. Rashid, S. Uddin, M.K. Khan, M.N. Khan, S. Ahmad, A.H.A. Ateya, M. A. ElAffendi, Analysis of Ca^{2+} substitution on the phase, microstructural and dielectric properties of $Ba_{1-x}Ca_x(Zn_{1/3}Nb_{2/3})O_3$ ceramics, Eng. Rep. 7 (7) (2025) e70234, https://doi.org/10.1002/eng2.70234.
[17] H. Naceur, A. Megriche, M. El Maaoui, Structural distortion and dielectric properties of $Sr_{1-x}(Na_{0.5}Bi_{0.5})_xBi_2Nb_2O_9$ (x= 0.0, 0.2, 0.5, 0.8 and 1.0), J. Alloys Compd. 546 (2013) 145–150, https://doi.org/10.1016/j.jallcom.2012.08.101.
[18] Y. Zhang, W. Li, Z. Wang, Y. Qiao, H. Xia, R. Song, Y. Zhao, W. Fei, Perovskite $Sr_{1-x}(Na_{0.5}Bi_{0.5})_xTi_{0.99}Mn_{0.01}O_3$ thin films with defect dipoles for high energy-storage and electrocaloric performance, ACS Appl. Mater. Interfaces 11 (41) (2019) 37947–37954, https://doi.org/10.1021/acsami.9b14815.
[19] I. Jalafi, S. El Barkany, Z. Bahari, M. Abou-salama, Structural, electrical, and dielectric study of the influence of 3.4% lanthanide (Ln^{3+}= Sm^{3+} and La^{3+}) insertion in the A-site of perovskite $Ba_{0.95}Ln_{0.034}Ti_{0.99}Zr_{0.01}O_3$, RSC Adv. 12 (2022) 33124–33141, https://doi.org/10.1039/d2ra06758g.
[20] G. Yuheng, Preparation of high-performance Bi-YG ferrite based on LTCC technology and theoretical analysis of its sintering mechanism, Ceram. Int. 50 (19) (2024) 34816–34823, https://doi.org/10.1016/j.ceramint.2024.06.290. Part A.
[21] M. Abbas, R. Ullah, K. Ullah, F. Sultana, A. Mahmood, A. Mateen, Y. Zhang, A. Ali, K. Althubeiti, M. Mushtaq, Structural, optical, electrical and dielectric properties of $(Sr_{1-x}Mg_x)(Sn_{0.5}Ti_{0.5})O_3$ (x= 0.00, 0.25, 0.50, 0.75) ceramics via solid state route, Ceram. Int. 47 (21) (2021) 30129–30136, https://doi.org/10.1016/j.ceramint.2021.07.191.
[22] C.J. Bartel, C. Sutton, B.R. Goldsmith, R. Ouyang, C.B. Musgrave, L.M. Ghiringhelli, M. Scheffler, New tolerance factor to predict the stability of perovskite oxides and halides, Sci. Adv. 5 (2) (2019) eaav0693, https://doi.org/10.1126/sciadv.aav0693.
[23] H.S. Mohanty, A. Kumar, B. Sahoo, P.K. Kurliya, D.K. Pradhan, Impedance spectroscopic study on microwave sintered (1-x)$Na_{0.5}Bi_{0.5}TiO_3$-x$BaTiO_3$ ceramics, J. Mater. Sci. Mater. Electron. 29 (2018) 6966–6977, https://doi.org/10.1007/s10854-018-8683-2.
[24] M. Basak, M.L. Rahman, M.F. Ahmed, B. Biswas, N. Sharmin, The use of X-ray diffraction peak profile analysis to determine the structural parameters of cobalt ferrite nanoparticles using Debye-Scherrer, Williamson-Hall, Halder-Wagner and Size-strain plot: different precipitating agent approach, J. Alloys Compd. 895 (2022) 162694, https://doi.org/10.1016/j.jallcom.2021.162694.
[25] V. Mote, Y. Purushotham, B. Dole, Williamson-Hall analysis in estimation of lattice strain in nanometer-sized ZnO particles, J. Theor. Appl. Phys. 6 (2012) 1–8, https://doi.org/10.1186/2251-7235-6-6.
[26] P.P. Ma, X.Q. Liu, F.Q. Zhang, J.J. Xing, X.M. Chen, Sr$(Ga_{0.5}Nb_{0.5})_{1-x}Ti_xO_3$ low loss microwave dielectric ceramics with medium dielectric constant, J. Am. Ceram. Soc. 98 (8) (2015) 2534–2540, https://doi.org/10.1111/jace.13655.
[27] A. Zhang, H. Fan, D. Hou, F. Yang, Y. Chen, W. Wang, W. Dong, A novel low-loss (1-x)$(Ca_{0.8}Sr_{0.2})TiO_{3-x}SmAlO_3$ microwave dielectric ceramics with near-zero temperature coefficient, J. Alloys Compd. 898 (2022) 162809, https://doi.org/10.1016/j.jallcom.2021.1628-09.
[28] L. Venkidu, D. Jain Ruth, M. Veera Gajendra Babu, P. Esther Rubavathi, D. Dhayanithi, N. Giridharan, B. Sundarakannan, Suppression of intermediate antiferroelectric phase in sub-micron grain size $Na_{0.5}Bi_{0.5}TiO_3$ ceramics, J. Mater. Sci. Mater. Electron. 33 (33) (2022) 25006–25024, https://doi.org/10.1007/s10854-022-09209-2.
[29] M. Benyoussef, M. Zannen, J. Belhadi, B. Manoun, J.-L. Dellis, A. Lahmar, M. El Marssi, Complex impedance and Raman spectroscopy of $Na_{0.5}(Bi_{1-x}Dy_x)_{0.5}TiO_3$ ceramics, Ceram. Int. 46 (8) (2020) 10979–10991, https://doi.org/10.1016/j.ceramint.2020.01.114.
[30] J. Mallick, A. Shukla, S.K. Panda, S.K. Biswal, S.N. Rout, M.K. Yadav, M. Kar, Crystal symmetry transition and its influence on optical, dielectric, and ferroelectric properties in (1-x)$Na_{0.5}Bi_{0.5}TiO_3$-x$SrTiO_3$ system, J. Alloys Compd. 978 (2024) 173403, https://doi.org/10.1016/j.jallcom.2023.173403.
[31] P.P. Ma, X.M. Chen, Further ordering structural investigation of Ba((Co,Zn,Mg)$_{1/3}Nb_{2/3})O_3$ perovskites by Raman spectroscopy, Mater. Char. 158 (2019) 109938, https://doi.org/10.1016/j.matchar.2019.109938.
[32] D. Rout, K.-S. Moon, V.S. Rao, S.-J.L. Kang, Study of the morphotropic phase boundary in the lead-free $Na_{1/2}Bi_{1/2}TiO_3$-$BaTiO_3$ system by Raman spectroscopy, J. Ceram. Soc. Jpn. 117 (1367) (2009) 797–800, https://doi.org/10.2109/jcersj2.117.797.
[33] C.-L. Diao, C.-H. Wang, N.-N. Luo, Z.-M. Qi, T. Shao, Y.-Y. Wang, J. Lu, Q.-C. Wang, X.-J. Kuang, L. Fang, First-principle calculation and assignment for vibrational spectra of Ba $(Mg_{1/3}Nb_{2/3})O_3$ microwave dielectric ceramic, J. Appl. Phys. 115 (11) (2014) 114103, https://doi.org/10.1063/1.4868226.
[34] S. Chauhan, M. Kar, J. Kumar, S.K. Jaiswal, Cerium induced Raman spectra of $(Ba_{0.5}Sr_{0.5})(Fe_{1-x}Ce_x)O_{3-\delta}$ (x=0-1), Mater. Chem. Phys. 241 (2020) 122378, https://doi.org/10.1016/j.matchemphys.2019.122378.
[35] K. Kannan, K.B. Tan, Z. Zainal, C.C. Khaw, S.K. Chen, O.J. Lee, Novel cadmium substituted barium zinc niobate perovskites: phase formation, structural and impedance studies, Results Phys. 19 (2020) 103374, https://doi.org/10.1016/j.rinp.2020.103374.
[36] K. Parmar, N. Negi, Influence of Na/Bi excess on structural, dielectric and multiferroic properties of lead free $(Na_{0.5}Bi_{0.5})_{0.99}La_{0.01}Ti_{0.988}Fe_{0.012}O_3$ ceramic, J. Alloys Compd. 618 (2015) 781–787, https://doi.org/10.1016/j.jallcom.2014.07.138.
[37] I. Levin, T. Amos, J. Nino, T.A. Vanderah, C. Randall, M. Lanagan, Structural study of an unusual cubic pyrochlore $Bi_{1.5}Zn_{0.92}Nb_{1.5}O_{6.92}$, J. Solid State Chem. 168 (1) (2002) 69–75, https://doi.org/10.1006/jssc.2002.9681.
[38] Z. Yao, R. Chu, Z. Xu, J. Hao, W. Li, G. Li, Processing and enhanced electrical properties of $Sr_{1-x}(K_{0.5}Bi_{0.5})_xBi_2Nb_2O_9$ lead-free piezoelectric ceramics, Ceram. Int. 42 (9) (2016) 10619–10623, https://doi.org/10.1016/j.ceramint.2016.03.156.
[39] S. Zhang, B.-p. Zhang, S. Li, Z. Huang, C. Yang, H. Wang, Enhanced photocatalytic activity in ag-nanoparticle-dispersed $BaTiO_3$ composite thin films: role of charge transfer, J. Adv. Ceram. 6 (2017) 1–10, https://doi.org/10.1007/s40145-016-0209-x.
[40] S. Nekipelov, O. Petrova, A. Koroleva, M. Krzhizhanovskaya, N. Zhuk, XPS study of pyrochlore type $Bi_2Cu_{1/3}Ni_{1/3}Co_{1/3}M_2O_{9\pm\delta}$ (M-Nb, Ta), Ceram. Int. 51 (3) (2024) 3343–3349, https://doi.org/10.1016/j.ceramint.2024.11.311.
[41] J. Heo, Y. Roh, K. Shin, C. Lee, C. Wang, H.-T. Kim, Versatile Zn hosting Lewis-basic interfacial layer for high-performant Zn reversibility in aqueous Zn ion battery, Energy Storage Mater. 71 (2024) 103580, https://doi.org/10.1016/j.ensm.2024.103580.
[42] K.S. Samantaray, P. Maneesha, R. Saha, K. Harrabi, A. Mekki, S. Sen, Composition and electric field driven studies on modified NBT-based lead-free ceramics, Mater. Sci. Eng. B 300 (2024) 117140, https://doi.org/10.1016/j.mseb.2023.117140.
[43] J. Fan, K. Du, Z.-Y. Zou, C.-Z. Yin, Y.-B. Guo, F. Wang, Q. Zhao, X.-H. Wang, W.-Z. Lu, W. Lei, Impedance spectroscopy, B-site cation ordering and structure–property relations of (1−x)La$[Al_{0.9}(Mg_{0.5}Ti_{0.5})_{0.1}]O_3$–x$CaTiO_3$ ceramics for 5G dielectric waveguide filters, Ceram. Int. 47 (11) (2021) 15319–15327, https://doi.org/10.1016/j.ceramint.2021.02.097.
[44] Q. Ji, L. Bi, J. Zhang, H. Cao, X.S. Zhao, The role of oxygen vacancies of ABO_3 perovskite oxides in the oxygen reduction reaction, Energy Environ. Sci. 13 (5) (2020) 1408–1428, https://doi.org/10.1039/D0EE00092B.
[45] W. Guo, Y. Lu, Z. Ma, H. Wu, Z. Yue, Defect-related broadband dielectric loss mechanisms of $Na_{1/2}Sm_{1/2}Ti_{1-z}(Al_{1/2}Nb_{1/2})_zO_3$ ceramics, Acta Mater. 255 (2023) 119093, https://doi.org/10.1016/j.actamat.2023.119093.
[46] H. Tian, Y. Zhang, R. Wang, H. Wu, L. Shan, Effect of Ge^{4+}-substituted on the structure characteristics and microwave/terahertz dielectric properties of ultra-low ε_r, high Q· f cordierite ceramics, J. Mater. Sci. Technol. 216 (2024) 165–177, https://doi.org/10.1016/j.jmst.2024.08.008.
[47] R.D. Shannon, Dielectric polarizabilities of ions in oxides and fluorides, J. Appl. Phys. 73 (1) (1993) 348–366, https://doi.org/10.1063/1.353856.
[48] E.S. Kim, B.S. Chun, R. Freer, R.J. Cernik, Effects of packing fraction and bond valence on microwave dielectric properties of $A^{2+}B^{6+}O_4$ (A^{2+}: ca, Pb, Ba; B^{6+}: mo, W) ceramics, J. Eur. Ceram. Soc. 30 (7) (2010) 1731–1736, https://doi.org/10.1016/j.jeurceramsoc.2009.12.018.
[49] D. Liang, Y. Li, X. Zhang, Z. Xiong, B. Tang, F. Si, Z. Fang, H. Li, Z. Shi, J. Chen, Crystal structure, Raman spectra, and microwave dielectric properties of a novel temperature-stable $LiY_9Si_6O_{26}$ ceramic with hexagonal structure, Ceram. Int. 49 (22) (2023) 36831–36837, https://doi.org/10.1016/j.ceramint.2023.09.013.
[50] R.D. Shi, L. Liu, X.L. Zhu, X.M. Chen, Ordered domain engineering and physical property modification of Ba$(Co_{1/3}Nb_{2/3})O_3$ complex perovskite ceramics, J. Am. Ceram. Soc. 105 (2) (2022) 1159–1172, https://doi.org/10.1111/jace.18145.
[51] A.R. West, D.C. Sinclair, N. Hirose, Characterization of electrical materials, especially ferroelectrics, by impedance Spectroscopy, J. Electroceram. 1 (1) (1997) 65–71, https://doi.org/10.1023/A:1009950415758.
[52] H. Li, X. Li, F. Liu, X. Lin, S. Liu, Effect of lattice defects on crystal structure and microwave properties of Ba$(Ga_{1/2}Ta_{1/2})O_3$ doped Ba$(Zn_{1/3}Nb_{2/3})O_3$ ceramics, J. Alloys Compd. 1002 (2024) 175175, https://doi.org/10.1016/j.jallcom.2024.175175.
[53] J.T.S. Irvine, D.C. Sinclair, A.R. West, Electroceramics: characterization by impedance spectroscopy, Adv. Mater. 2 (3) (1990) 132–138, https://doi.org/10.1002/adma.19900020304.
[54] S. Fei Liu, Y. Jun Wu, J. Li, X. Ming Chen, Effects of oxygen vacancies on dielectric, electrical, and ferroelectric properties of $Ba_4Nd_2Fe_2Nb_8O_{30}$ ceramics, Appl. Phys. Lett. 104 (8) (2014) 082912, https://doi.org/10.1063/1.4867069.
[55] G. Singh, V.S. Tiwari, P.K. Gupta, Role of oxygen vacancies on relaxation and conduction behavior of $KNbO_3$ ceramic, J. Appl. Phys. 107 (6) (2010) 064103, https://doi.org/10.1063/1.3309745.
[56] T.-F. Zhang, X.-G. Tang, Q.-X. Liu, Y.-P. Jiang, X.-X. Huang, Oxygen-vacancy-related high temperature dielectric relaxation in $(Pb_{1-x}Ba_x)ZrO_3$ ceramics, J. Am. Ceram. Soc. 98 (2) (2015) 551–558, https://doi.org/10.1111/jace.13317.